Biosensors and Bioelectronics 129 (2019) 124–131

Contents lists available at ScienceDirect

Biosensors and Bioelectronics

journal homepage: www.elsevier.com/locate/bios

A novel sandwich-type photoelectrochemical immunosensor based on Ru(bpy)$_3^{2+}$ and Ce-CdS co-sensitized hierarchical ZnO matrix and dual-inhibited polystyrene@CuS-Ab$_2$ composites

Dawei Fan*, Xin Liu, Chunzhu Bao, Jinhui Feng, Huan Wang, Hongmin Ma, Dan Wu, Qin Wei

Key Laboratory of Interfacial Reaction & Sensing Analysis in Universities of Shandong, School of Chemistry and Chemical Engineering, University of Jinan, Jinan 250022, PR China

ARTICLE INFO

Keywords:
Hierarchical ZnO microsphere
Ru(bpy)$_3^{2+}$
Cerium-doped cadmium sulfide
Polystyrene@CuS
β-amyloid protein

ABSTRACT

A novel and sensitive sandwich-type photoelectrochemical (PEC) immunosensor was developed for the quantitative detection of β-amyloid protein (Aβ). A ITO electrode was sequentially coated with hierarchical porous zinc oxide (ZnO) microspheres with a large specific area, sensitized with tris(bipyridine)ruthenium(II) ion (Ru(bpy)$_3^{2+}$) to achieve high visible light absorption, and modified with cerium-doped cadmium sulfide (Ce-CdS) nanoparticles to enhance the PEC response. Under the stimulation of visible light and ascorbic acid as an efficient electron donor, the photoelectric signal of ZnO/Ru(bpy)$_3^{2+}$/Ce-CdS was 70 times that of pure ZnO. The amino-functionalized polystyrene (PS) microspheres coated with copper sulfide (CuS) was linked with a secondary antibody (Ab$_2$) for the first time for the Aβ detection by the immunosensor. The good insulation and steric resistance of the as-prepared polystyrene@CuS-Ab$_2$ (PS@CuS-Ab$_2$) composite significantly weakened the photocurrent response of the immunosensor in the specific immune recognition. Under the optimal conditions, the quantitative detection of Aβ was achieved within the range of 0.001–100 ng/mL with the detection limit of 0.37 pg/mL. In addition, the PEC immunosensor is easy to make, stable and selective, which has provided a good experimental platform for the detection of disease biomarkers.

1. Introduction

Photoelectrochemical (PEC) sensor is target recognition technique based on the photoelectric properties of electrode materials. Many semiconductor nanomaterials have been used for the fabrication of PEC sensors. Semiconductor nanomaterials have advantages of good chemical stability, large specific surface area, environmentally friendly material, high activity and low cost (Fan et al., 2018; Li et al., 2017a; Soltani et al., 2018; Yang and Li, 2008). ZnO is a wide band-gap (3.37 eV) semiconductor nanomaterial (Chen et al., 2018b; Hernández-Carrillo et al., 2018; Jiang et al., 2018; Schrier et al., 2007; Wang et al., 2019), and its performance is significantly affected by the phase structure, specific surface area and crystallinity (Lee et al., 2010; Loh et al., 2015; Tong et al., 2018). In the present work based on the method reported in literature (Yan et al., 2017), we synthesized hierarchical porous ZnO microspheres with the diameter of 3 μm and high specific surface area to facilitate the composition with other materials.

Ru(bpy)$_3^{2+}$ can exhibit good physical and chemical properties as combined with semiconductor materials by a series of reactions in electrolytes. Ru(II) complexes tend to be oxidized to Ru(III) complexes. The reaction between the Ru(III) complexes and semiconductor materials can form an excited state of Ru(II)*. The excited state further returns to the ground state via electron transfer and energy transfer, leading to a strong electrochemiluminescence (ECL) emission (Chen et al., 2018a; Ji et al., 2017; Moretto et al., 2010; Wang et al., 2017; Zhang et al., 2017). In our work, the hierarchical porous ZnO microspheres were sensitized with Ru(bpy)$_3^{2+}$ to enhance the PEC response.

The selection and preparation of semiconductor materials have always been a hot topic in the field of photoelectricity. CdS has a narrow band-gap (2.4 eV) with strong visible light absorption (Guo et al., 2017; Wessendorf et al., 2018; Yu et al., 2017). Its PEC activity can be significantly enhanced by cerium doping (Chen et al., 2018c; Feng et al., 2018; Li et al., 2017c; Liu et al., 2017; Tsai et al., 2010). In the present work, Ce-CdS was in-situ grown on the ZnO/Ru(bpy)$_3^{2+}$ composite to further enhance the photoelectric signal.

To obtain an ultrasensitive PEC immunosensor, the sandwich-type sensor and signal amplification strategy were adopted in the present work. The Ab$_2$ of Aβ was immobilized on PS@CuS. PS have many

* Corresponding author.
E-mail address: jndxfandawei@126.com (D. Fan).

https://doi.org/10.1016/j.bios.2019.01.029
Received 30 October 2018; Received in revised form 30 December 2018; Accepted 8 January 2019
Available online 21 January 2019
0956-5663/

advantages, such as the perfect geometrical shape, uniform particle size and strong surface reactivity (Liu et al., 2012; Nehache et al., 2017; Yu et al., 2018; Zhao et al., 2018). CuS has a direct band-gap of 2.0 eV. Due to the strong absorption ability of exciting light, CuS will allow the transfer of less light energy to the substrate. An appropriate electron receptor (O_2 dissolved in electrolyte) can capture photo-generated e^- of CuS under illumination (Liu et al., 2013; Wang et al., 2013; Zhang et al., 2012), and the h^+ in the valence band (VB) is easily neutralized by the electron donors. The combination of the insulation properties of PS and the strong light absorption capacity of CuS can enhance the properties of the dual-inhibited ultrasensitive PEC immunosensor.

Aβ is the most important biomarker for the diagnosis of Alzheimer's disease. The highly sensitive detection of serum Aβ is crucial for the early diagnosis. Herein, based on the strategies discussed above, a novel sandwich-type PEC immunosensor was prepared with ZnO/Ru$(bpy)_3^{2+}$/Ce-CdS composite and PS@CuS labeled secondary antibodies (PS@CuS-Ab_2), and its performance in the detection of Aβ was evaluated.

2. Experimental

2.1. Materials and reagents

Zinc sulfate heptahydrate, cerium(III) nitrate hexahydrate and copper(II) chloride dihydrate were purchased from the Chinese Medicine Group Chemical Reagent Co., Ltd (Shanghai, China). Cadmium nitrate tetrahydrate was obtained from Shanghai McLean Biochemistry Technology Co., Ltd (Shanghai, China). The information of other materials can be found in Electronic supporting information (ESI).

2.2. Apparatus

PEC tests were conducted with a CHI760E electrochemical workstation (Chenhua Instrument Shanghai Co., Ltd, China). A 100 W LED lamp of white light was used as the irradiation source. The detailed procedure for the test can be found in ESI.

2.3. Synthesis of hierarchical ZnO microspheres

Hierarchical ZnO microspheres were prepared by a hydrothermal and calcination method reported in literature (Yan et al., 2017), The detailed procedure is described in ESI.

2.4. Preparation of PS@CuS-Ab_2 bioconjugates

Fig. 1A shows the schematic preparation process of PS@CuS-Ab_2. Typically, 54 mg copper chloride and 80 mg trisodium citrate were dissolved in 350 mL ultrapure water, and then mixed with 1 mL of 4 mg/mL sodium sulfide. The mixture solution was magnetically stirred for 5 min and heated at 90 °C for 15 min to afford CuS quantum dots (Xie et al., 2014; Zhang et al., 2016). A PS suspension (200 μL) was dispersed into the CuS quantum dots solution (100 mL) and stirred at 120 °C for 2 h. The mixture was centrifuged and the residue was dispersed into 2 mL ultrapure water to give a PS@CuS suspension.

The as-prepared PS@CuS suspension (200 μL) was dispersed into 1 mL of the freshly prepared EDC (0.01 mol/L)/NHS (0.002 mol/L) solution and oscillated 30 min to activate the carboxyl group of PS@CuS. The mixture was then incubated with 2 mL of 1 μg/mL Ab_2 solution at 4 °C for 12 h and centrifuge. The residue was then incubated with 1 mL of 0.1% bovine serum albumin (BSA) on a shaker at room temperature for 1 h and centrifuged to block the nonspecific binding sites. The PS@CuS-Ab_2 composite was then dispersed in 2 mL ultrapure water and stored at 4 °C (Fan et al., 2017; Wang et al., 2018) for further use.

2.5. Construction of PEC immunosensor

Fig. 1B shows the schematic construction procedure of the PEC immunosensor. Firstly, 4 mg/mL ZnO suspension was dispersed with ultrasonic for 1 min. Then, the 10 μL of ZnO suspension was dropped onto a clean and dried ITO electrode and dried in air. 4 μL of 0.03 mol/L Ru$(bpy)_3^{2+}$ solution was then coated on the surface of the above electrode for 30 min and washed off with ultrapure water. The electrode was dried at room temperature in the dark, and then coated with 4 μL of 0.08 mol/L $Cd(NO_3)_2$ and 0.005 mol/L $Ce(NO_3)_3$ mixture at room temperature for 30 min. Ce-CdS layer was then grown on the sequentially coated electrode with 4 μL of 0.1 mol/L Na_2S solution at room temperature for 30 min. The electrode was rinsed with ultrapure water and dried to form an ITO/ZnO/Ru$(bpy)_3^{2+}$/Ce-CdS electrode that was then sequentially coated at room temperature with 4 μL of 1 mol/L thioglycolic acid (TGA) for 30 min, then the excess TGA was removed by ultrapure water. Soon after, 4 μL of EDC (0.01 mol/L)/NHS (0.002 mol/L) was trickled onto the electrode and incubated for 1 h, followed by rinsing with ultrapure water to remove the unreacted EDC/NHS. Then, 4 μL of 1 μg/mL Aβ-antibody (Ab_1) was coated on the electrode surface, incubated at room temperature for about 30 min, and washed with ultrapure water to remove the unbound Ab_1. The non-

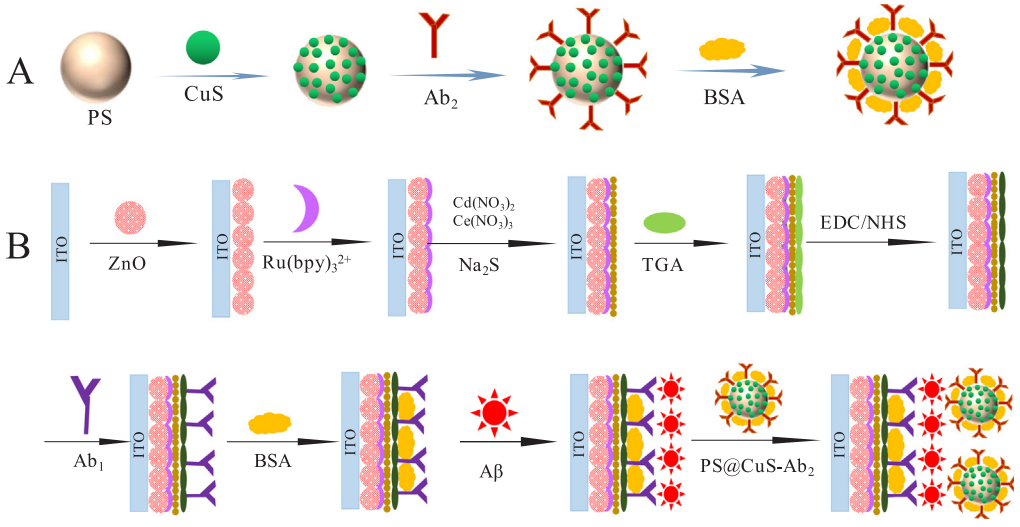

Fig. 1. The preparation process of the second antibody incubator (A) and the construction process of the PEC immunosensor (B).

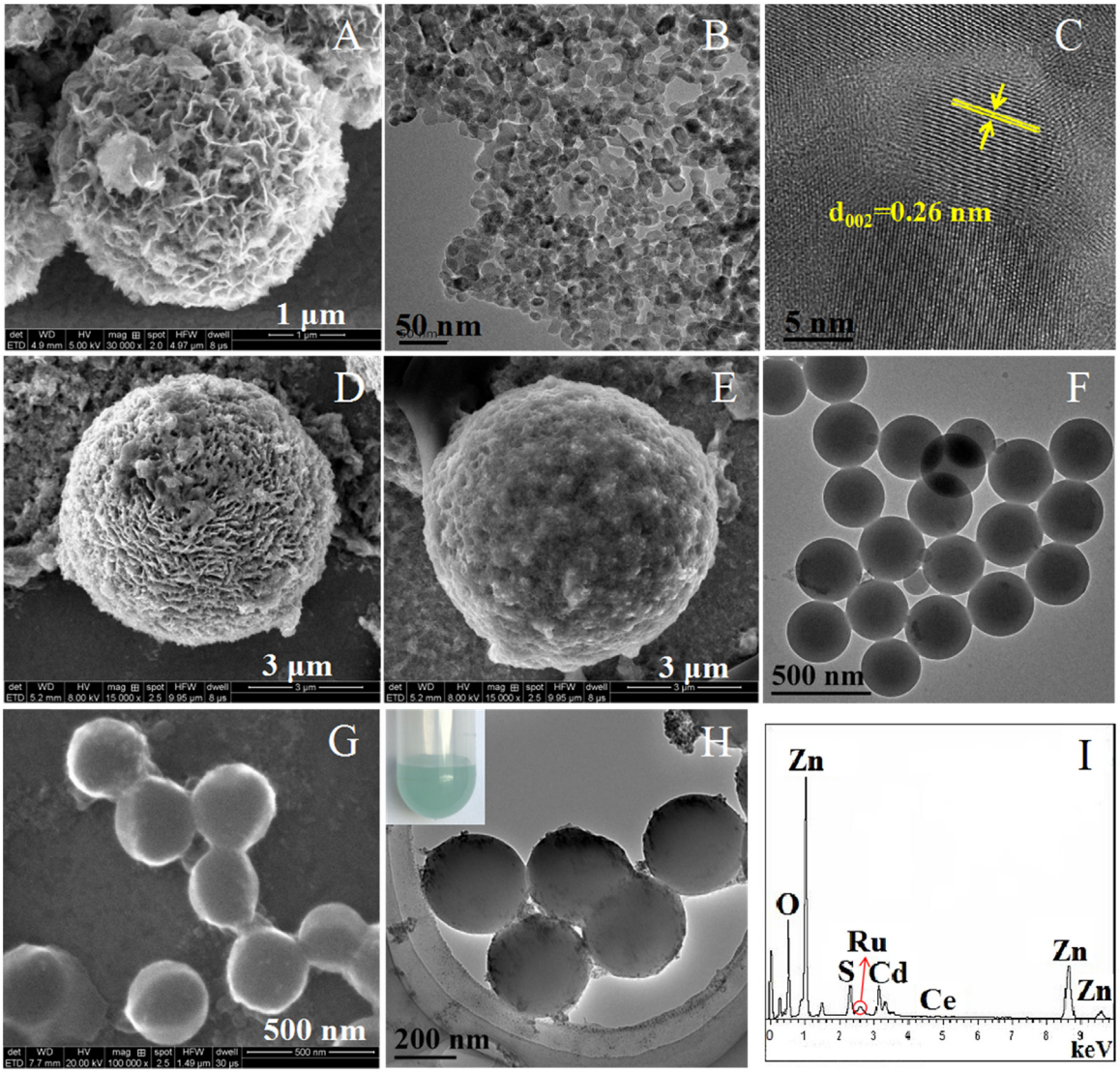

Fig. 2. SEM (A), TEM (B) and HR-TEM (C) images of ZnO, SEM (D) image of ZnO/Ru(bpy)$_3^{2+}$, SEM (E) image of ZnO/Ru(bpy)$_3^{2+}$/Ce-CdS, TEM (F) image of pure PS, SEM (G) and TEM (H) image of PS@CuS, EDS (I) images of ZnO/Ru(bpy)$_3^{2+}$/Ce-CdS. Inset in H shows the photograph of the PS@CuS suspension.

specific binding sites was blocked with 4 μL of 0.1% BSA solution for 30 min. Subsequently, the Aβ of different concentrations (4 μL) was modified on the electrode surface, which was incubated for 30 min at room temperature, and the unbound antigen was washed with ultrapure water. Finally, the electrodes respectively reacted with 4 μL of PS@CuS-Ab$_2$ suspension at room temperature for 30 min, and rinsed with ultrapure water. The ITO/ZnO/Ru(bpy)$_3^{2+}$/Ce-CdS/TGA/(EDC/NHS)/Ab$_1$/BSA/Aβ/PS@CuS-Ab$_2$ electrodes were obtained.

3. Results and discussion

3.1. Characterization of the synthesized materials

The morphologies and elemental composition of the synthesized materials were analyzed by scanning electron microscopy (SEM), transmission electron microscope (TEM) and energy dispersive spectroscopy (EDS). The synthesized ZnO are regular spheres with a hierarchical nano-lamellar structure, which is favorable to the growth of composite nanoparticles with superior properties (Fig. 2A). The high magnification TEM image of the lamellar structure of ZnO revealed a distinct porous sheet structure (Fig. 2B). Clear and uniform lattice fringes with the spacing of 0.26 nm were observed by HR-TEM (Fig. 2C), corresponding to the (002) crystal planes of hexagonal wurtzite ZnO (Liu et al., 2011; Qin et al., 2016; Shi et al., 2015). The coating layer on the electrode gradually became thicker as sequentially coated with Ru(bpy)$_3^{2+}$ and Ce-CdS (Fig. 2D and E), suggesting that the substrate material ZnO/Ru(bpy)$_3^{2+}$/Ce-CdS was successfully prepared. The TEM image of pure PS microspheres suggests that they are uniform microparticles with smooth surfaces (Fig. 2F). Fig. 2G, Fig. 2H and Fig. S1 (ESI†) show the SEM and TEM images of PS@CuS, respectively. It is clear that the CuS nanoparticles have been successfully composed with the PS microspheres, indicating that the PS@CuS has been successfully synthesized. So, it is favorable for the efficient attachment of Aβ to PS@CuS surface. Inset in Fig. 2H shows the good dispersion of PS@CuS suspension. The EDS image of ZnO/Ru(bpy)$_3^{2+}$/Ce-CdS (Fig. 2I) further confirmed that Ru(bpy)$_3^{2+}$ and Ce-CdS were successfully coated on the surface of the hierarchical porous ZnO microspheres.

Fig. 3A shows the X-ray diffraction (XRD) patterns of the substrate materials. The peaks of ZnO can be indexed to the hexagonal phase ZnO (PDF#36-1451). The diffraction peaks of Ru(bpy)$_3$Cl$_2$ were also found in the ZnO/Ru(bpy)$_3^{2+}$ and the ZnO/Ru(bpy)$_3^{2+}$/Ce-CdS composite. The diffraction peaks of CdS were indexed to hexagonal pure CdS crystal (PDF#10–0454). The XRD pattern of Ce-CdS did not change compared with pure CdS, and the diffraction peak of cerium species was

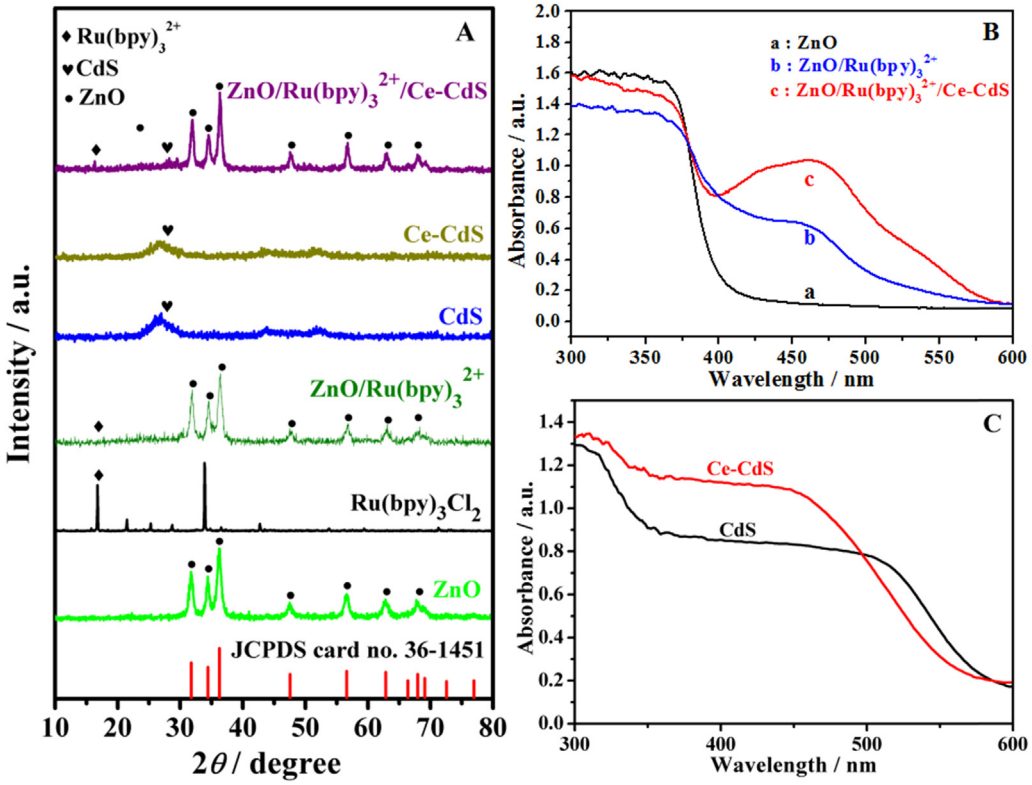

Fig. 3. XRD pattern of ZnO, $Ru(bpy)_3Cl_2$, ZnO/$Ru(bpy)_3^{2+}$, CdS, Ce-CdS, ZnO/$Ru(bpy)_3^{2+}$/Ce-CdS (A). UV–vis diffuse reflectance spectra of (B) ZnO (a), ZnO/$Ru(bpy)_3^{2+}$ (b), ZnO/$Ru(bpy)_3^{2+}$/Ce-CdS (c) and (C) Ce-CdS, CdS.

not obtained, which could be caused by the small quantity of cerium-doped CdS. The UV–vis diffuse reflectance spectroscopy analysis shows that the ZnO microspheres mainly absorb lights with the wavelength shorter than 400 nm, and thus the visible light utilization efficiency of ZnO is very low (Fig. 3B). The ZnO/$Ru(bpy)_3^{2+}$/Ce-CdS composite exhibited strong absorption in the whole visible region, indicating that the composite material could be used to significantly improved the visible light utilization efficiency (Fig. 3B). The UV–vis absorption spectra of CdS and Ce-CdS further suggest that the substrate material has been successfully prepared (Fig. 3C).

3.2. Characterization of the fabricated novel PEC immunosensor

To confirm the successful preparation of the sandwich-type PEC immunosensor, the photocurrent response of a series of electrodes (Fig. 4A) and the electrochemical impedance spectroscopy (EIS) Nyquist diagram (Fig. 4D) were investigated. At the same time, as an ideal electron donor, ascorbic acid (AA) was used to remove the photo-generated pores and suppress the e^-/h^+ combination, thereby obtaining an excellent and stable PEC signal of the immunosensor.

Fig. 4A illustrates the photocurrent-time curves of the PEC sensors fabricated in each step for Aβ detection. The response of bare ITO electrode (curve a) to visible light is very weak, and the photocurrent signal is almost zero. After surface modification with ZnO (curve b), the electrode has a certain response to light, the photocurrent signal was improved, but still relatively low. After sensitization of $Ru(bpy)_3^{2+}$ (curve c) on the surface of ZnO, the photocurrent was increased, and the mechanism of sensitizing ZnO with $Ru(bpy)_3^{2+}$ is as follows (Chi et al., 2007; Hong et al., 2017; Hou et al., 2012; Moretto et al., 2010):

$$Ru(bpy)_3^{2+} - e^- \rightarrow Ru(bpy)_3^{3+} \quad (1)$$

$$Ru(bpy)_3^{3+} \xrightarrow{ZnO} [Ru(bpy)_3^{2+}]^* \quad (2)$$

$$[Ru(bpy)_3^{2+}]^* \rightarrow Ru(bpy)_3^{2+} + hv \quad (3)$$

The Ru(II) complexes was oxidized to Ru(III) complex (1). The reaction between Ru(III) complex and ZnO composite resulted in an excited state of $Ru(II)^*$ (2) that returned to the ground state via electron transfer, leading to a strong ECL emission (3). The in-situ growth of Ce-CdS on the surface of the $Ru(bpy)_3^{2+}$-sensitized ZnO further increased the photocurrent from 0.7 μA to 22 μA (curve d). It can be explained that the bandgap edge and valence band of Ce-CdS are higher than those of ZnO which is favorable for the electron transfer from Ce-CdS to ZnO. The coating with TGA further increased the photocurrent to 30 μA (curve e). The sulfhydryl group of TGA have certain reducing effect, which could contribute to reduction of photo-generated hole (h^+) and the separation photo-generated/electron (h^+/e^-). After modified by EDC/NHS, the photocurrent decreased significantly (curve f). As a classic amidation reagent, the EDC/NHS solution was used to link the –COOH group of TGA and $–NH_2$ group of Anti-Aβ. Subsequently, Ab_1, BSA and Aβ were sequentially clustered on the electrode, the signal was continuously decreased (curve g, h and i), this is because the assembly of these proteins on modified electrodes blocks the diffusion of AA to the light of the photoactive matrix, and obscures some of the excitation light (Zhao et al., 2012). Finally, as the steric hindrance and competitive effect of the PS@CuS-Ab_2 (curve j), the photocurrent was significantly reduced after specific immune recognition, which proved the successful construction of the sandwich-type PEC immunosensor.

The layer-by-layer assembly of the PEC immunosensor was further characterized with EIS using $[Fe(CN)_6]^{3-/4-}$ as a redox probe. All of the EIS Nyquist plots of modified electrodes of each step are composed of a semicircle in the high frequency region and a linear plot in the low frequency region (Fig. 4D). The inset shows the corresponding Randles equivalent circuit consisting of the resistance of solution (R_s), the charge transfer resistance (R_{ct}), the double layer capacitance (C_{dl}) and the Warburg impedance (Z_W). The value of R_{ct} varies with the modification of the working electrode, which is reflected by the diameter of

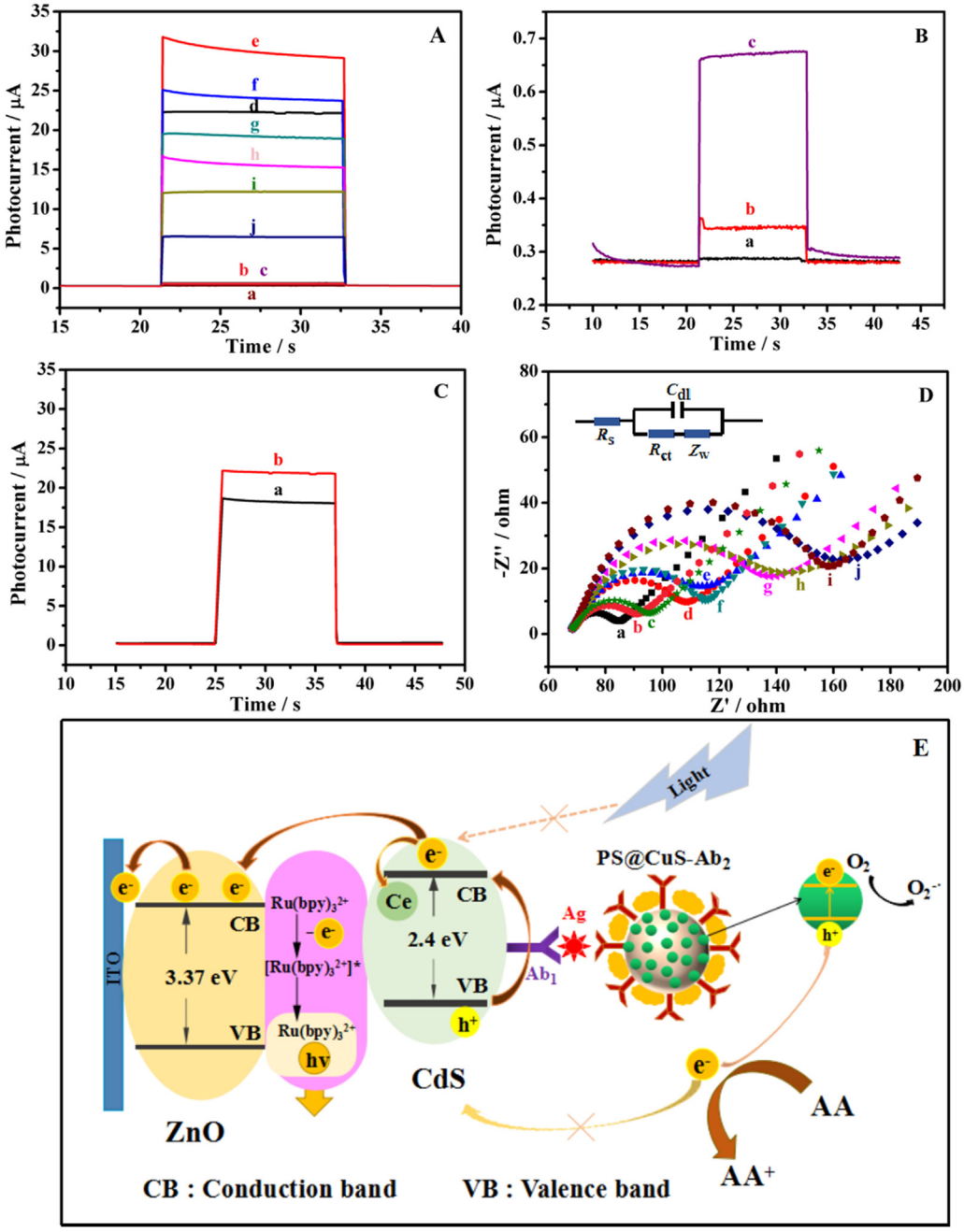

Fig. 4. (A) and (B) Time-based photocurrent response curves and (D) EIS Nyquist plots of (a) ITO, (b) ITO/ZnO, (c) ITO/ZnO/$Ru(bpy)_3^{2+}$, (d) ITO/ZnO/$Ru(bpy)_3^{2+}$/ Ce-CdS, (e) ITO/ZnO/$Ru(bpy)_3^{2+}$/Ce-CdS/TGA, (f) ITO/ZnO/$Ru(bpy)_3^{2+}$/Ce-CdS/ TGA/(EDC/NHS), (g) ITO/ZnO/$Ru(bpy)_3^{2+}$/Ce-CdS/TGA/(EDC/NHS)/Ab_1, (h) ITO/ZnO/$Ru(bpy)_3^{2+}$/Ce-CdS/TGA/(EDC/NHS)/Ab_1/BSA, (i) ITO/ZnO/$Ru(bpy)_3^{2+}$ /Ce-CdS/TGA/(EDC/NHS)/Ab_1/BSA/Aβ, (j) ITO/ZnO/$Ru(bpy)_3^{2+}$/Ce-CdS/TGA/ (EDC/NHS)/Ab_1/BSA/Aβ/PS@CuS-Ab_2. The applied potential is 0 V and the concentration of Aβ is 1 ng/mL. PEC signals of (a) ITO/ZnO/$Ru(bpy)_3^{2+}$/CdS and (b) ITO/ZnO/$Ru(bpy)_3^{2+}$/Ce-CdS (C). Electron transfer mechanism of sandwitch-type PEC immunosensor (E).

the semicircle in the EIS Nyquist plot. It is clear that R_{ct} increased gradually as the electrode sequentially coated for constructing the PEC immunosensor (Table S1 (ESI)), The bare ITO electrode is conductive, and thus exhibits a low R_{ct} (curve a). The modification with ZnO increased the R_{ct} (curve b), The modifications of ITO/ZnO electrode with $Ru(bpy)_3^{2+}$ (curve c) and Ce-CdS (curve d) increased the impedance. The TGA coating (curve e) slightly increased R_{ct} because the organic TGA molecules impeded the electrode transfer. The insulation layer of EDC/NHS further increased R_{ct} (curve f). The successive modification of the ITO/ZnO/$Ru(bpy)_3^{2+}$/Ce-CdS/TGA/EDC/NHS electrode with Ab_1 (curve g), BSA (curve h) and Aβ (curve i) gradually increased the R_{ct} because of the insulation properties. The R_{ct} further increased as the PS@CuS-Ab_2 (curve j) was due to the strong steric hindrance and insulation properties of PS@CuS. These results further demonstrate that the sandwich-type PEC immunosensor can be used for the sensitive detection of Aβ.

3.3. PEC mechanism of the immunoassay

Based on these experimental results, the electron transfer mechanism of the sandwich-type PEC immunosensor in AA electrolyte was proposed (Fig. 4E). It has been well demonstrated that the photophysical and electronic properties of a semiconductors can be altered by metal doping (He et al., 2017; Novakova et al., 2018). The band-gap of ZnO is 3.37 eV, which makes the photo-generated electrons/holes under the illumination of visible light very difficult. The sensitization of the ZnO with $Ru(bpy)_3^{2+}$ was able to enhance the PEC response. Furthermore, the doped Ce^{3+} in CdS depressed the electron annihilation obviously, resulting from the formation of a new energy band-gap in the middle of CdS. The gradient was effectively accelerated the electron transfer rate. Besides, the Ce-CdS nanoparticles exhibited stronger visible light absorption than pure CdS semiconductor (Fig. 3C), which also contributed to the high PEC response. However, as the bioconjugates, a competitor of light energy, the CuS blocked the light from the

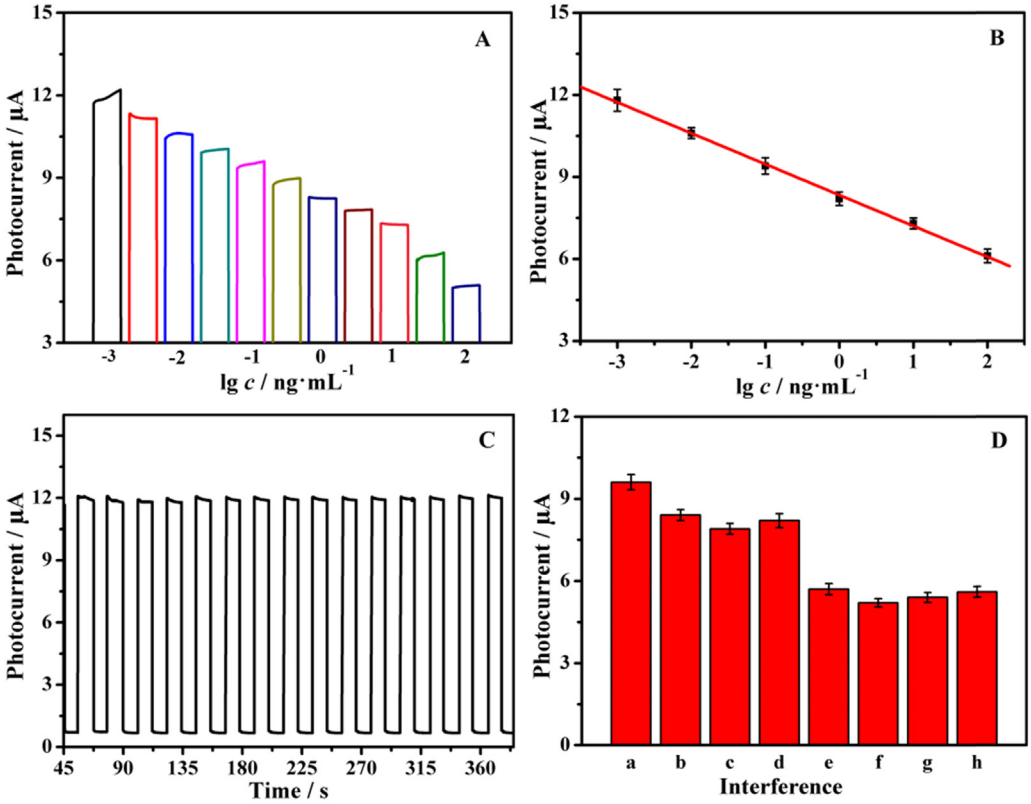

Fig. 5. (A) Photocurrent response and (B) the logarithmic calibration curve for PEC immunosensor to detect Aβ with different concentrations. (C) Photocurrent response of the PEC immunosensor under 10 on/off illumination cycles for 380 s, $c_{Aβ}$ = 1 ng/mL. (D) Selectivity of the PEC immunosensor to detect Aβ. (a) Blank, (b) Blank + 100 ng/mL SCCA, (c) Blank + 100 ng/mL NT-proBNP, (d) Blank + 100 ng/mL cTnI, (e) 1 ng/mL Aβ, (f) 1 ng/mL Aβ + 100 ng/mL SCCA, (g) 1 ng/mL Aβ + 100 ng/mL NT-proBNP, (h) 1 ng/mL Aβ + 100 ng/mL cTnI. The applied potential was 0 V.

photoactive matrix due to its strong light trapping properties. In Addition, the E_{CB} of CuS is more negative than that of $O_2/O_2^{-\cdot}$ (−0.33 eV versus NHE) (Scheme S1), and thus the electron acceptor (O_2) in the electrolyte can capture the e^- (CB) of the irradiated CuS and convert it into superoxide anion radicals ($O_2^{-\cdot}$) active species. The holes left in VB were then captured by AA (Li et al., 2017b). The oxidative $O_2^{-\cdot}$ then reacted with the reductive AA in near-neutral electrolyte, producing AA^+ and H_2O, which further consumed AA. The reduced AA then decreased the efficiency of holes scavenging and thus induce charge carriers recombination of ZnO/Ru$(bpy)_3^{2+}$/Ce-CdS photoactive matrix, leading to the declined photocurrents. The large specific surface area and good biocompatibility of PS make it a suitable carrier to increase the Ab_2 loading amount of CuS. In addition to functioning as a carrier, the non-conductive PS also dramatically increased the steric hindrance of the sensing electrode and suppressed the electron transfer from AA to the ZnO/Ru$(bpy)_3^{2+}$/Ce-CdS sensitized structure, which further aggravated the PEC damping effect. In all, the synergistic effect mentioned above endowed immunosensor the high sensitivity for the insulin detection.

3.4. Optimization of experimental conditions

The experimental conditions including the concentrations of Ru$(bpy)_3^{2+}$, AA, $Ce(NO_3)_3$ and pH were optimized for reaching high performances for the detection of Aβ (Fig. S2, ESI). The highest photocurrent was achieved at the Ru$(bpy)_3^{2+}$ concentration of 0.03 mol/L (Fig. S2A). The visible light absorption of the ZnO/Ru$(bpy)_3^{2+}$/Ce-CdS substrate increased with the increase of AA concentration from 0.02 mol L^{-1} to 0.1 mol L^{-1}, and remained almost constant as the AA concentration further increased. Therefore, the AA concentration was optimized as 0.1 mol/L (Fig. S2B). In pH 7.4 PBS solution, the optimal photocurrent signal was obtained (Fig. S2C). Therefore, pH 7.4 PBS solution was selected as the optimal pH environment. Fig. S2D showed that with the increase of $Ce(NO_3)_3$ concentration, when the concentration increases to 0.005 mol/L, the photocurrent rises to the highest level. Therefore, we selected $Ce(NO_3)_3$ solution with concentration of 0.005 mol/L for further study.

3.5. PEC analysis for Aβ

The novel PEC electrodes modified with different concentrations of Aβ was carried out in the optimal conditions. From the Fig. 5A, as the concentrations of Aβ increased, the photocurrent reduced gradually because of the insulation properties of Aβ, which indicated the prepared PEC immunosensor was appropriate for Aβ detection. In addition, the photocurrent reduced linearly with the logarithm of Aβ concentration range from 0.001 ng/mL to 100 ng/mL (Fig. 5B). The linear equation was I= 12.29–1.131 lg ($c_{Aβ}$, ng/mL) with a correlation coefficient of 0.998. The detection limit was 0.37 pg/mL.

Fig. 5C demonstrated the photocurrent response of the immunosensor modified with 1 ng/mL Aβ under 10 times on/off illumination cycles for 380 s. Over time, there was no obvious variation in the photoelectric current, indicating the good stability of the prepared PEC immunosensor. The reproducibility of the PEC sensor was studied by five electrodes with 1 ng mL^{-1} of Aβ, the photocurrents were 9.25 μA, 8.62 μA, 8.48 μA, 9.11 μA and 8.84 μA, respectively. The relative standard deviation (RSD) was calculated as 1.2%, which illustrated that the PEC immunosensor was precise and reproducible.

Fig. 5D shows the selective detection of Aβ ground photoelectric sensor, which verifies its practicability. The photocurrent signals were investigated by blending 1 ng/mL of Aβ with 100 ng/mL of SCCA, 100 ng/mL NT-ProBNP and 100 ng/mL cTnI. After 100 ng/mL of SCCA, NT-ProBNP or cTnI was incubated on the blank electrode (ZnO/Ru$(bpy)_3^{2+}$/Ce-CdS/TGA/(EDC/NHS)/Ab_1/BSA/PS@CuS-Ab_2) either mixed with Aβ or not, there was no evident change of photocurrent signal. The results illustrated the fabricated PEC immunosensor possessed excellent specificity and selectivity for Aβ detection.

Table 1
Comparison of different methods for the detection of Aβ.

Method	Linear range (ng/mL)	Detection limit (pg/mL)	Reference
PEC sensor	0.001–100	0.37	This method
ELISA	0–0.25	6.25	(Esparza et al., 2013)
Cyclic Voltammetry	0.5–500	100	(Rama et al., 2014)
Microarray Immune	0–5	73.07	(Gagni et al., 2013)
CIEF	2–50	200	(Haußmann et al., 2013)
Electrochemical Impedance Spectroscopy	0.01–1	5.2	(Carneiro et al., 2017)
Surface Enhancement of Raman scattering	0–0.006	0.5	(Demeritte et al., 2015)

3.6. Comparison of various methods for Aβ detection

To further validate the novel sandwich-type PEC immunosensor, the comparison of different methods for the detection of Aβ was shown in Table 1. The satisfactory results revealed the promising application of the fabricated PEC immunosensor in blood sample detection.

4. Conclusion

In conclusion, a sandwich-structured PEC immunosensor with excellent photoelectric properties was prepared by the modification with hierarchical porous ZnO microspheres with a larger surface area, sensitization with $Ru(bpy)_3^{2+}$, and in-situ growth of Ce-CdS composite sequentially. PS@CuS-Ab_2 composite was prepared by coating Ab_2 on PS@CuS microspheres with strong steric hindrance and good insulation properties for the specific recognition between the antigen and antibody. The as-prepared PEC immunosensor exhibited high sensitivity and selectivity for the detection of Aβ in the broad range of 0.001–100 ng/mL and a low detection limit of 0.37 pg/mL. This novel, sensitive and stable PEC sensor is a promising immunosensor candidate with great application prospects for the early diagnosis and in the field of photoelectrochemical.

CRediT authorship contribution statement

Dawei Fan: Conceptualization, Data curation, Formal analysis, Writing - original draft, Writing - review & editing. **Xin Liu:** Data curation, Formal analysis, Writing - original draft, Writing - review & editing. **Chunzhu Bao:** Data curation, Formal analysis, Writing - original draft. **Jinhui Feng:** Writing - review & editing. **Huan Wang:** Writing - review & editing. **Hongmin Ma:** Writing - review & editing. **Dan Wu:** Writing - review & editing. **Qin Wei:** Conceptualization.

Acknowledgments

This research was financially supported by the National Key Scientific Instrument and Equipment Development Project of China (No. 21627809), the National Natural Science Foundation of China (Nos. 21775054, 21675063 and 21575050), the Natural Science Foundation of Shandong Province of China (Nos. ZR2017BB030 and ZR2016JL013), and QW thanks the Special Foundation for Taishan Scholar Professorship of Shandong Province (No. ts20130937) and UJN.

Author contributions

D.W.F. and Q.W. made the conceptualization. D.W.F., X.L. and C.Z.B performed the date curation and formal analysis, and writed the original draft. D.W.F., X.L., J.H.F, H.W, H.M.M and D. W. contributed substantially to review and editing. All the authors discussed the results and commented on the manuscript.

Declaration of interests

None.

Appendix A. Supplementary material

Supplementary data associated with this article can be found in the online version at doi:10.1016/j.bios.2019.01.029.

References

Carneiro, P., Loureiro, J., Delerue-Matos, C., Morais, S., Pereira, M.D.C., 2017. Sens. Actuators B 239, 157–165.
Chen, C., Wei, G., Yao, X., Liao, F., Peng, H., Zhang, J., Hong, N., Cheng, L., Fan, H., 2018a. J. Solid State Electrochem. 1–8.
Chen, W., Wu, W., Yang, W., Zhao, J., Xiao, M., Kong, W., 2018b. Int. J. Hydrog. Energy 43, 9969–9977.
Chen, X., Hu, Z., Cao, M., Hu, C., Liu, S., Chen, H., Shi, Y., Kou, H., Xie, T., Vedda, A., 2018c. J. Eur. Ceram. Soc. 38, 3246–3254.
Chi, Y., Dong, Y., Chen, G., 2007. Anal. Chem. 79, 4521–4528.
Demeritte, T., Nellore, B.P., Kanchanapally, R., Sinha, S.S., Pramanik, A., Chavva, S.R., Ray, P.C., 2015. ACS Appl. Mater. Interfaces 7, 13693–13700.
Esparza, T.J., Zhao, H., Cirrito, J.R., Cairns, N.J., Bateman, R.J., Holtzman, D.M., Brody, D.L., 2013. Ann. Neurol. 73, 104–119.
Fan, D., Bao, C., Liu, X., Wu, D., Zhang, Y., Wang, H., Du, B., Wei, Q., 2018. J. Mater. Chem. B 7634–7642.
Fan, D., Xiang, R., Wang, H., Dan, W., Di, Z., Chen, Y., Qin, W., Du, B., 2017. Biosens. Bioelectron. 87, 593–599.
Feng, J., Li, F., Li, X., Wang, Y., Fan, D., Du, B., Li, Y., Wei, Q., 2018. Biosens. Bioelectron. 117, 773–780.
Gagni, P., Sola, L., Cretich, M., Chiari, M., 2013. Biosens. Bioelectron. 47, 490–495.
Guo, X., Chen, Y., Qin, Z., Su, J., Guo, L., 2017. Chemcatchem 10, 153–158.
Haußmann, U., Jahn, O., Linning, P., Janßen, C., Liepold, T., Portelius, E., Zetterberg, H., Bauer, C., Schuchhardt, J., Knölker, H.J., 2013. Anal. Chem. 85, 8142–8149.
He, Z., Li, M., Que, W., Stang, P.J., 2017. Dalton Trans. 46, 3120–3124.
Hernández-Carrillo, M.A., Torres-Ricárdez, R., García-Mendoza, M.F., Ramírez-Morales, E., Rojas-Blanco, L., Díaz-Flores, L.L., Sepúlveda-Palacios, G.E., Paraguay-Delgado, F., Pérez-Hernández, G., 2018. Catal. Today. https://doi.org/10.1016/j.cattod.2018.04.060.
Hong, L.R., Zhao, J., Lei, Y.M., Yuan, R., Zhuo, Y., 2017. Electrochim. Acta 241, 291–298.
Hou, J.G., Hu, F.T., Cao, Y.T., Jin, H.J., Li, T.H., Gan, N., 2012. Adv. Mater. Res. 345, 381–386.
Ji, X., Li, D., Wang, Z., Tan, M., Huang, H., Deng, G., 2017. Eur. J. Org. Chem. 2017, 6652–6659.
Jiang, H., Zhang, X., Gu, W., Feng, X., Zhang, L., Weng, Y., 2018. Chem. Phys. Lett. 711, 100–106.
Lee, S.H., Han, S.H., Jung, H.S., Shin, H., Lee, J., Noh, J.H., Lee, S., Cho, I.S., Lee, J.K., Kim, J., 2010. J. Phys. Chem. C. 114, 7185–7189.
Li, H., He, X., Xiao, H.J., Du, H., Wang, J., Zhang, H., 2017a. Phys. Chem. Chem. Phys. 19, 28056–28062.
Li, R., Zhang, Y., Tu, W., Dai, Z., 2017b. ACS Appl. Mater. Interfaces 9, 22289–22297.
Li, Z., Wang, W., Zhao, Z., Liu, X., Song, P., 2017c. RSC Adv. 7, 28366–28372.
Liu, D., Qi, H., Cheng, B., 2012. J. Mater. Eng. 2 (4), 1–4.
Liu, S., Li, C., Yu, J., Xiang, Q., 2011. Crystengcomm 13, 2533–2541.
Liu, Y., Zou, J., Shi, M., Yang, B., Han, Y., Li, W., Wang, Z., Zhou, H., Li, M., Jiang, N., 2017. Ceram. Int. 44, 1091–1098.
Liu, Z., Han, J., Han, L., Guo, K., Li, Y., Cui, T., Wang, B., Liang, X., 2013. Mater. Chem. Phys. 141, 804–809.
Loh, L., Briscoe, J., Dunn, S., 2015. ACS Appl. Mater. Interfaces 7, 152–157.
Moretto, L.M., Kohls, T., Badocco, D., Pastore, P., Sojic, N., Ugo, P., 2010. J. Electroanal. Chem. 640, 35–41.
Nehache, S., Semsarilar, M., In, M., Dieudonnégeorge, P., Laikeehim, J., Bron, P., Bouyer, D., Deratani, A., Quemener, D., 2017. Polym. Chem. 8, 3357–3363.
Novakova, V., Donzello, M.P., Ercolani, C., Zimcik, P., Stuzhin, P.A., 2018. Coord. Chem. Rev. 361, 1–73.
Qin, J., Zhang, X., Yang, C., Cao, M., Ma, M., Liu, R., 2016. Appl. Surf. Sci. 392, 196–203.
Rama, E.C., González-García, M.B., Costa-García, A., 2014. Sens. Actuators B 201,

567–571.
Schrier, J., Demchenko, D.O., Wang, L.W., Alivisatos, A.P., 2007. Nano Lett. 7, 2377–2382.
Shi, L., Lin, L., Wang, F., Liu, M., Sun, J., 2015. J. Mater. Sci. 50, 1718–1727.
Soltani, T., Tayyebi, A., Lee, B.K., 2018. Appl. Surf. Sci. 448, 465–473.
Tong, Y., Jiang, T., Qiu, S., Koshmak, K., Giglia, A., Kubsky, S., Bendounan, A., Chen, L., Pasquali, L., Esaulov, V.A., 2018. J. Phys. Chem. C 122, 2880–2889.
Tsai, C.C., Chung, C.H., Wang, J., Cheng, W.C., Chen, M.H., Liou, J.S., Chang, J.K., Hsu, Y. C., Hung, S.C., Lee, C.W., 2010. High thermal stability of high-power phosphor based white-light-emitting diodes employing Ce:YAG-doped glass, in: Proc. - Electron. Compon. Technol. Conf., pp. 700–703.
Wang, B.S., Li, R.Y., Zhang, Z.Y., Xing-Wang, Wu, X.L., Cheng, G.A., Zheng, R.T., 2019. Catal. Today 321–322, 100–106.
Wang, Q., An, N., Bai, Y., Hang, H., Li, J., Lu, X., Liu, Y., Wang, F., Li, Z., Lei, Z., 2013. Int. J. Hydrog. Energy 38, 10739–10745.
Wang, X., Gao, P., Yan, T., Li, R., Xu, R., Zhang, Y., Du, B., Wei, Q., 2018. Sens. Actuators B 258, 1–9.
Wang, Y., Zhao, G., Li, X., Liu, L., Cao, W., Wei, Q., 2017. Biosens. Bioelectron. 101, 290–296.
Wessendorf, C.D., Hanisch, J., Müller, D., Ahlswede, E., 2018. Sol. RRL 2. https://doi.org/10.1002/solr.201800056.
Xie, Y., Yan, B., Xu, H., Jian, C., Liu, Q., Deng, Y., Zeng, H., 2014. ACS Appl. Mater. Interfaces 6, 8845–8852.
Yan, B., Wang, Y., Jiang, X., Liu, K., Liang, G., 2017. ACS Appl. Mater. Interfaces 9, 29113–29119.
Yang, C.C., Li, S., 2008. J. Phys. Chem. B 112, 14193–14197.
Yu, J., Lee, T.I., Misra, M., 2018. J. Ind. Eng. Chem. 66, 468–477.
Yu, Z., Kumar, M.R., Chu, Y., Hao, H., Wu, Q., Xie, H., 2017. ACS Sustain. Chem. Eng. 6, 155–164.
Zhang, L., Sun, Y., Liang, Y.Y., He, J.P., Zhao, W.W., Xu, J.J., Chen, H.Y., 2016. Biosens. Bioelectron. 85, 930–934.
Zhang, L., Tian, K., Dong, Y., Ding, H., Wang, C., 2017. Analyst 143, 304–310.
Zhang, Y., Tian, J., Li, H., Wang, L., Qin, X., Asiri, A.M., Alyoubi, A.O., Sun, X., 2012. Langmuir 28, 12893–12900.
Zhao, Q., Piao, J., Peng, W., Wang, Y., Zhang, B., Gong, X., Chang, J., 2018. ACS Appl. Mater. Interfaces 10, 3324–3332.
Zhao, W.W., Ma, Z.Y., Yu, P.P., Dong, X.Y., Xu, J.J., Chen, H.Y., 2012. Anal. Chem. 84, 917–923.